Review

Recent progress in metallic glasses in Taiwan

J.C. Huang [a,*], J.P. Chu [b], J.S.C. Jang [c]

[a] Department of Materials and Optoelectronic Science, Center for Nanoscience and Nanotechnology, National Sun Yat-Sen University, Kaohsiung 80424, Taiwan, ROC
[b] Department of Polymer Engineering, National Taiwan University of Science and Technology, Taipei 10607, Taiwan, ROC
[c] Department of Materials Science and Engineering, I-Shou University, Kaohsiung 84001, Taiwan, ROC

ARTICLE INFO

ABSTRACT

The recent research and development on metallic glasses in Taiwan over the past decade is reviewed in this paper. The major focus was to develop tougher bulk metallic glasses (BMGs), bulk metallic glass composites (BMGCs), and thin film metallic glasses (TFMGs), mostly in Zr and Mg based systems. Due to the Taiwan industry characteristics, metallic glasses are favored in the application for micro-electro-mechanical systems (MEMS), including micro- or nano-imprinting for optoelectronic devices and hologram patterns.

© 2009 Elsevier Ltd. All rights reserved.

1. Introduction

Metallic glasses have been one of the extensive research subjects over the past twenty years. The unique properties such as high strength and hardness, special damping property, soft magnetic characteristics, and oxidation/corrosion resistance enable this new category of metallic materials to be applied for structural or functional applications. Before 1990s the research and development (R&D) focuses of metallic glasses were mainly on the Au–Si and Pd based system. After the breakthrough in early 1990s, many other systems such as La, Mg, and Zr based bulk metallic glasses (BMGs) were developed. So far, the existing and on-going efforts have developed numerous successful systems, including Zr, Fe, Mg, Au, Pd, Pt, Cu, Ni, Ti, Co, Al, Ce, Ca, La, and many other rare-earth based amorphous alloys, as reviewed in a number of review papers [1–5].

In addition to the metallic glasses in the bulk form, recently, metallic glasses have been extended to the thin or thick film area, in an attempt to find applications in the micro-electro-mechanical systems (MEMS). For such applications, the amorphous alloys sometimes need to be fabricated via the sputtering or other thin film processes. The as-deposited thin film metallic glasses (TFMGs) usually exhibit a uniform composition without micro-segregation, avoiding the possible local crystallization during the fabrication process.

The initial R&D activities of the BMGs and TFMGs in Taiwan start from early 1990s, in academic university such as National Tsing-Hua University and National Taiwan Ocean University, as well as in research institutes such as Industry Technology Research Institute (ITRI) and Chung-Shan (Military) Institute of Science and Technology. The initial R&D was aimed on the Zr, Mg and Fe based BMGs. Later research was continuously extended in several universities, such as National Sun Yat-Sen University, I-Shou University and National Taiwan Ocean University, together with the reinforcement from Metal Industries Research & Development Centre (MIRDC). The major joint efforts were lunched in 2000s. An international collaboration project on metallic glasses was approved in 2005, covering eight research laboratories in National Sun Yat-Sen University, National Taiwan Ocean University, I-Shou University, National Cheng-Kung University and National Taiwan University of Science and Technology, as well four USA laboratories in Oak Ridge National Laboratory, University of Tennessee, and University of Wisconsin, Madison. MIRDC was also involved to promote industry applications.

2. Alloy design

The initial alloy design was limited to the Zr based BMGs [6–13]. Effects of individual micro-alloying with Si (0–10 at%) or B (0–4 at%) on the thermal properties of the $Zr_{65}Cu_{17.5}Ni_{10}Al_{7.5}$ base alloy have

been systematically investigated. It is found that the additions of both B and Si pose a positive effect on thermal stability of base alloys, while keeping the same glass-forming ability (GFA) as the base alloy. The largest activation energy of crystallization, about 360 kJ/mol, occurs at the compositions of $Zr_{63}Cu_{17.5}Ni_{10}Al_{7.5}B_2$ and $Zr_{61}Cu_{17.5}Ni_{10}Al_{7.5}Si_4$. Furthermore, the $Zr_{65-x-y}Al_{7.5}$ $Cu_{17.5}Ni_{10}Si_xB_y$ alloy system, where $x = 0-4$ and $y = 0-2$, was selected for studying the effect of simultaneously adding B (with a smallest atomic size) and Si (with a negative heat of mixing) on its crystallization and thermal stability. The experimental evidence and the kinetic analyses revealed that, with the addition of 4 at% Si and 1 at% B, the T_{rg} ($= T_g/T_l$) and γ ($= T_x/(T_g + T_l)$) (where T_g, T_x, and T_l are the glass transition, crystallization, and liquidus temperature, respectively) values increase from 0.57 and 0.40 for the $Zr_{65}Al_{7.5}Cu_{17.5}Ni_{10}$ base alloy to 0.62 and 0.43, suggesting the improved glass-forming ability. The saturation point for nucleation for 4%Si–1%B and 1%Si–2%B amorphous alloys occurs at the 88% crystallization fraction, much higher than the 65% for the base alloy [10–12], implying that these metalloid elements would extend the nucleation stage and result in smaller crystalline particles. Moreover, the variation of the incubation time, as shown in Fig. 1 [6], exhibits an increasing trend with increasing silicon addition, directly supporting that the Si addition would improve the thermal stability of the $Zr_{65}Al_{7.5}Cu_{17.5}Ni_{10}$ base alloy. Parallel studies have also been done on the $Zr_{53}Cu_{30}Ni_9Al_8$ amorphous alloy [13] which computationally designed by thermodynamics and deep eutectic methodology [14]. The improvement of thermal stability by the Si addition is contributed by the increase of their atomic packing density as well as their Zr–Si and Ni–Si strong atomic bonding, promoting the coating of Si thin layer on the nanocrystalline Zr_2Ni phase [6].

The $Mg_{65}Cu_{25-x}Gd_{10}Ag_x$ alloy system was systematically investigated to reveal the effect of Ag (in substituting Cu) on the GFA and crystallization behavior of the base alloy [15]. Because of a large difference in atomic size between Ag and the constituting elements the atomic radius of Ag is larger than that of Cu by 11% and is smaller than those of Mg and Gd by 10% and 19.5%, respectively, the atomic packing density of the $Mg_{65}Cu_{25-x}Gd_{10}Ag_x$ alloy would increase with increasing Ag content and concurrently increase its GFA. The highest γ value (0.407) and a relatively high T_{rg} (0.58) occur at the $Mg_{65}Cu_{22.5}Gd_{10}Ag_{2.5}$ alloy. More recently, new optimum alloy designs are made based on the recent model of optimum composition extension from the binary eutectic pairs, originally proposed by Lu et al. [14]. This model suggests that the optimum Mg based BMGs might possess a composition with

a lower amount of Mg and a higher amount of rare-earth (RE) element, for example, the $Mg_{58}Cu_{31}Y_{11}$ and $Mg_{58}Cu_{31}Gd_{11}$ [16,17]. A series of Mg based BMGs with 50–60 at% Mg and 10–15 at% dual RE elements (Nd and Y) are prepared by atmosphere-controlled induction melting and injection casting methods [18]. The selection of Nd for partially replacing Y element is inspired by the facts such as the difference between Nd and Y in covalent atomic radius (Nd: 0.164 nm; Y: 0.162 nm), electronegativity (Nd: 1.14, Y: 1.22), electronic configuration (Nd: $4f^45d^06s^2$, Y: $4d^15s^2$), and near-zero heat of mixing of the Y–Nd binary system (forming continuous solid solutions). These differences may result in certain change of short range ordering in the undercooled liquid of the $Mg_{58}Cu_{31}Y_{11-x}Nd_x$ alloys, favoring the glass formation. The recent results revealed that the highest γ value (0.414) and a relatively high T_{rg} (0.55) occur in the $Mg_{58}Cu_{31}Y_6Nd_5$ and $Mg_{58}Cu_{31}Y_4Nd_7$ alloys. In addition, a BMG rod with 10 mm in diameter can be produced for $Mg_{58}Cu_{31}Y_6Nd_5$ alloy by a Cu mold injection casting.

The effects of adding small-sized B to replace Cu or Y in the $Mg_{65}Cu_{25}Y_{10}$ based alloy have been examined [19]. It is found that the replacement of Y by B consistently leads to apparent degradation in GFA; the only large-sized Y seems to be irreplaceable. In contrast, the replacement of the small-sized Cu by the even smaller B to a small amount (1–5%) appears to be beneficial in terms of wider ΔT, higher GFA and hardness. The optimum quaternary alloy composition is located to be $Mg_{65}Cu_{22}Y_{10}B_3$. It is also found that the thermal stability and crystallization energy can be enhanced by the small addition of B [20].

Using the computational-thermodynamic approach, the potential compositions of Zr–Cu–Ni–Al alloy system, exhibiting the two-liquid miscibility phase equilibrium in the liquid temperature region, have been identified [21]. It was noted that the Zr–Cu–Ni–Al alloy system is a good candidate for this investigation, since it shows a high GFA and includes an atomic pair with a positive enthalpy of mixing between Ni and Cu elements (+4 kJ/mol). Since the positive heat of mixing between Cu and Ni is very slight, how to pinpoint the composition of an alloy exhibiting phase separation appears to be a scientific challenge. The Zr based bulk metallic glasses with the composition predicted by the thermodynamic calculations, $Zr_{63.8}Ni_{16.2}Cu_{15}Al_5$ for the 5% Al alloy series, show a microstructure of two micro-scaled glassy phases, as shown in Fig. 2 [21]. According to the solution thermodynamic principle, there are positive mixing-enthalpy values to induce the two-liquid miscibility region.
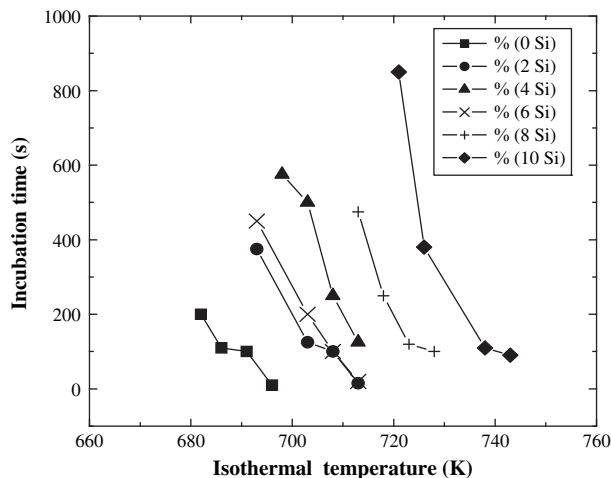

Fig. 1. Incubation time as a function of isothermal temperature for the $Zr_{65-x}Al_{7.5}Cu_{17.5}Ni_{10}Si_x$ alloys with Si content from 0 to 10 at% [6].
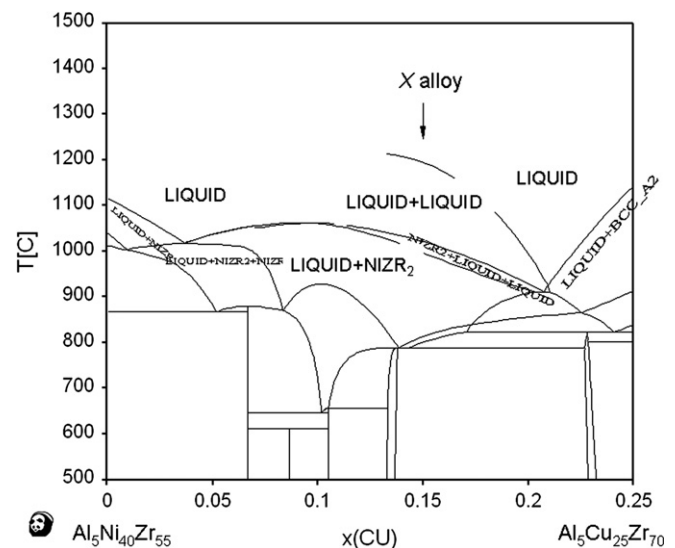

Fig. 2. The simulated phase diagram for the composition cut between $Al_5Ni_{40}Zr_{55}$ and $Al_5Cu_{25}Zr_{70}$ [21].
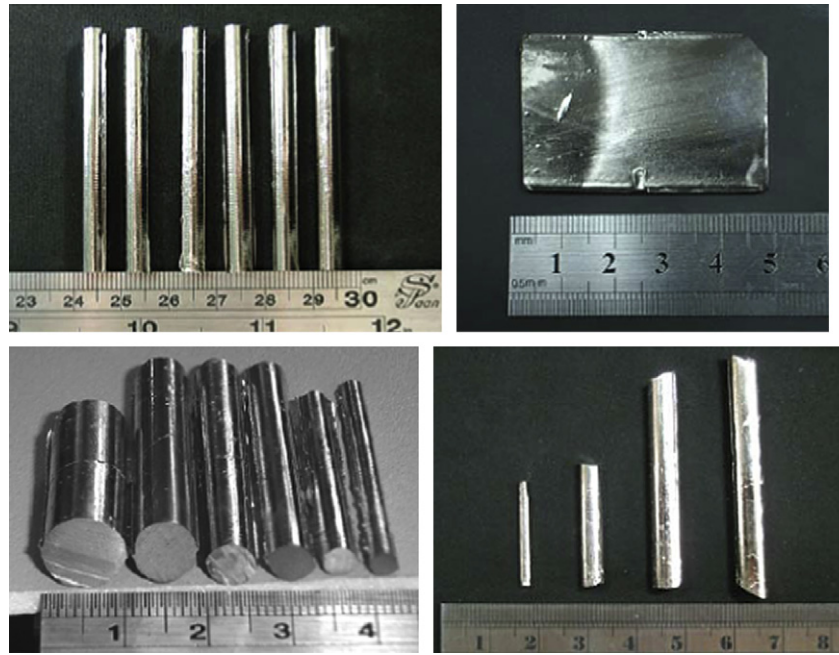
Fig. 3. Showing the Zr or Mg based BMG rods and plates in various dimensions.

The spinodal lines can be calculated based on the conditions that the second derivate of Gibbs free energy is equal to zero within the two-liquid miscibility region. In parallel studies using thermodynamic computations [22,23], such spinodal boundaries can be carefully established. The liquid composition within the spinodal region may decompose into two liquid phases assigned as Ni-rich liquid and Cu-rich liquid and form the two-liquid metallic glass. The designed alloy composition is selected, namely, $Zr_{65.8}Ni_{15.8}Cu_{8.4}Al_{10}$ for the 10% Al series. Both $Zr_{63.8}Ni_{16.2}Cu_{15}Al_5$ and $Zr_{65.8}Ni_{15.8}Cu_{8.4}Al_{10}$ lie within the spinodal region. It should be noted that all the predicted alloys have more Ni than Cu, different from most Zr based BMGs containing more Cu than Ni, as the typical one reported by Zhang et al. [24].

During the alloy design for optimum BMGs, the GFA index was also part of the study. There have been a number of indices to evaluate the glass-forming ability of BMGs, such as $\gamma \ (= T_g/T_x + T_l)$, T_x/T_l, $\Delta T_x \ (= T_x - T_g)$, $T_{rg} \ (= T_g/T_l)$, $T_x/(T_l - T_g)$, $T_g/T_l + T_x/T_g$ and $(T_x - T_g)/(T_l - T_g)$, where T_g is the glass transition temperature, T_x the crystallization temperature, and T_l the liquidus temperature. In 2007, it was further developed some more reliable parameters, one is $\gamma_m = (2T_x - T_g)/T_l$ [25,26], and the other is $\kappa = \Delta T_x/T_x + T_g/T_l$ [27]. The existing experimental data can be fit into the trend to confirm that the γ_m and κ parameters exhibit the best correlation with GFA among all parameters suggested so far for bulk metallic glasses, due to the fact that the new indicator considers all related factors for the liquid phase stability during cooling and the resistance to crystallization during heating.

Fe based soft magnetic BMGs have been studied by Chin and his coworkers in National Tsing Hua University [28–30]. A new simple ternary $Fe_{76}B_{20}Y_4$ BMG rod measuring 2 mm in diameter was developed with a high saturation magnetization of 1.56 T, low coercivity less than 40 A/m, and high electrical resistivity larger than 200 mV cm [28]. Other Fe based amorphous and nanocrystalline melt-spun ribbons with promising soft magnetic properties are continuously explored [29].

In addition, the new ternary Ni–Ta–Sn ternary BMG system was also developed, with $33 < Ta < 38$ and $2 < Sn < 9$ (in at%). The alloy shows a wide BMG forming regime. The crystallization temperature is among the highest in Ni based BMGs, with a wide supercooled
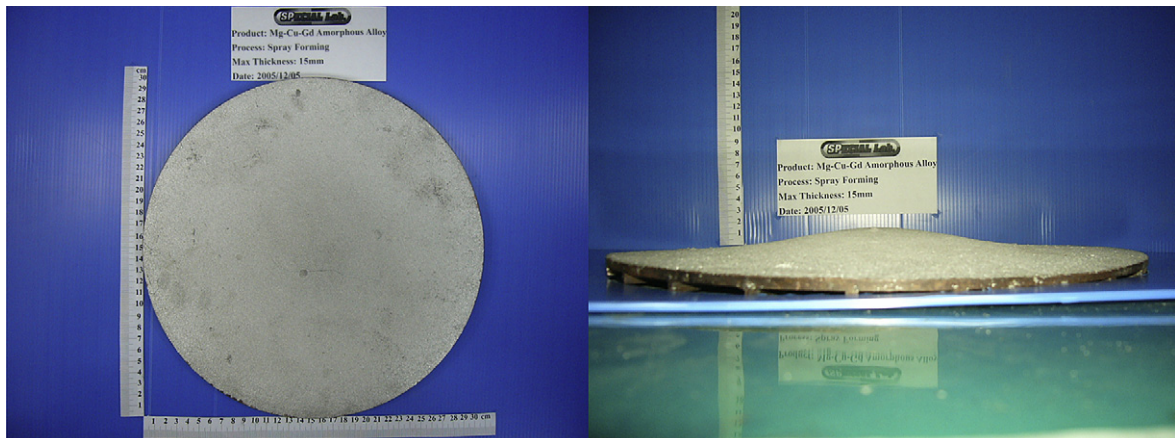

Fig. 4. Morphology of a spray-formed Mg–Cu–Gd layered composite plate with a Gaussian-shape, and 300 mm in diameter, 12 mm in maximum thickness, and 510 g in mass [40].
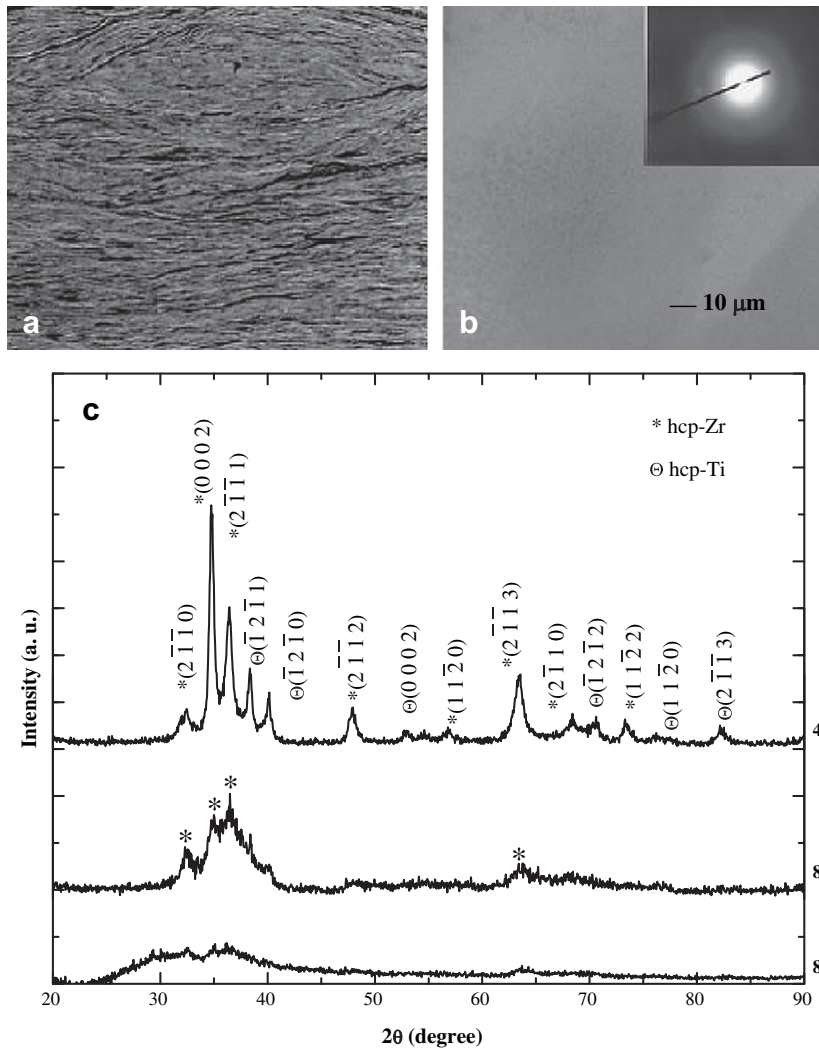
Fig. 5. (a) The stacked Zr and Ti foils after 50 ARB cycles, (b) typical TEM micrograph and electron diffraction pattern of the vitrified $Zr_{50}Ti_{50}$ region by ARB, and (c) typical XRD patterns of the ARB $Zr_{50}Ti_{50}$ samples after different cycles at room temperature [49].

liquid region 57–61 K. This Ni–Ta–Sn BMG shows high hardness, typically $H_v \sim 1000$, and a compressive fracture strength 856–1192 MPa. The $Ni_{58}Ta_{36}Sn_6$ BMG also exhibits good corrosion resistance in the anodic region [30].

The synthesis and characteristics of the Mg based BMG composites (BMGCs) have been studied in I-Shou University [31–35]. The Mg based BMGCs are fabricated through mechanical alloying (MA) in the planetary mill, using amorphous $Mg_{65}Cu_{25-x}Y_{10}Ag_x$
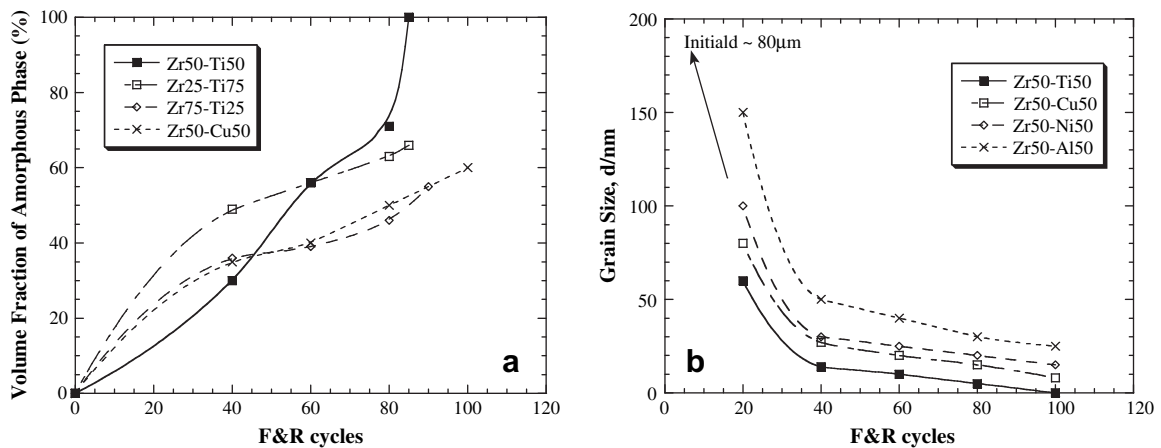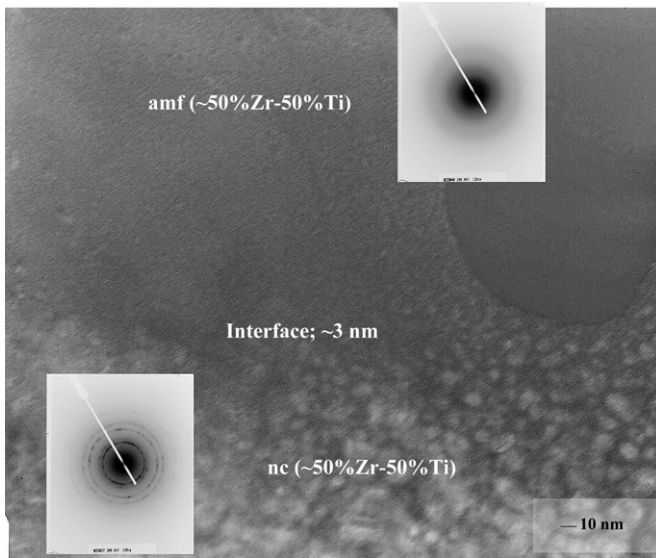

Fig. 6. The variations of (a) nanocrystalline grain size and (b) amorphous volume fraction in various Zr–X alloys as a function of ARB cycles, based on the X-ray diffraction results [51].

Fig. 7. TEM bright-field images of the interface region between the nanocrystalline and amorphous phases. The smallest nc phase size near the interface is around 3 nm [50].

($x = 0$, 5, 10) matrix alloy prepared by melt spinning and 1–5 vol% spherical nano-sized ZrO_2 particles. The melt-spun amorphous matrix ribbons are ground into powders and mixed with the ZrO_2 nano particles in the planetary mill, followed by hot pressing in Ar atmosphere under different pressures at the temperature 5 K above the glass transition temperature. Throughout the MA and hot pressing processes, the Mg based BMGCs exhibit an amorphous $Mg_{65}Cu_{20}Y_{10}Ag_5$ matrix microstructure with 80-nm nano ZrO_2 particles homogeneously dispersed. The microstructure near the interface between the matrix and nano particles presents a well-bonded condition. In addition, the hot-pressed composite can reach a 96% density, 360 in H_v hardness, and 700 MPa for the compressive strength. Moreover, the toughness of the Mg based BMGCs exhibit an increasing trend with increasing nano-sized ZrO_2 content, and can reach a level of 8.9 MPa m$^{0.5}$ [32,33].

3. Fabrication

The fabricating routes for the BMGs in I-Shou University and National Sun Yat-Sen University are either injection or suction casting, with arc or induction furnace. For producing the Zr based (or CuZr based) BMGs, an atmosphere-controlled arc-melting/suction casting process is the preferable way to prepare the Zr based alloys. The rods with dimension of 8 mm $\varphi \times 70$ mm L and plates with dimension of 3 mm $T \times 30$ mm $W \times 60$ mm L of the Zr based BMGs can be successfully fabricated by this method. On the other hand, for making the Mg based BMGs and BMGCs, two-steps atmosphere control induction melting and injection casting process is in use to prepare the highly reactive and high vapor-pressured Mg based alloys. The rods with dimension of 10 mm $\varphi \times 60$ mm L and plate with dimension of 2 mm $T \times 20$ mm $W \times 60$ mm L of the Mg based BMGs can be successfully prepared. Some examples are shown in Fig. 3.

Spray forming has also been applied to fabricate Al and Mg based amorphous plates measuring 1–10 mm in thickness in National Cheng-Kung University [36–40]. Spray forming can be considered as an intermediate processing between casting and deposition, with a cooling rate in the range of 1–100 K/s. Spray forming was firstly employed to fabricate $Al_{89}La_6Ni_5$ based BMGs and later Mg–Cu–Y or Mg–Cu–Gd systems, as shown in Fig. 4 [40].

BMGs and BMGCs have been fabricated using the mechanical alloying and consolidation methods [41–48]. Examples include the Mg and Ti based amorphous composites with additives of WC, SiC, carbon nanotube (CNT) powders. It is found that mechanical alloying may cause partial dissolutions of the additives, and thus the thermal stability of the amorphous matrix is altered due to the deviation in chemical composition of the glassy matrix. Yet, the supercooled liquid region of resulting materials remains almost unchanged. Compared with the pure amorphous structure, the hardness of the BMGCs increases as much as 30% due to the presence of additives. The composites suffer partial crystallization during the consolidation process in the supercooled liquid region.

The amorphous materials have also been prepared by accumulative roll bonding (ARB) via room-temperature cold rolling in the solid state for alternating thin layers of various metals with a special arrangement of composition [49–56]. Binary Zr–Ti, Zr–Ni, Zr–Cu and Zr–Al, ternary Zr–Cu–Ni, quaternary Zr–Cu–Ni–Ti and pentanary Zr–Cu–Ni–Ti–Al systems were systematically explored. It is found the crystalline foils can be mixed into homogeneous nanocrystalline and/or amorphous phase with increasing ARB cycles. After around 80–120 cycles, the alloys can be mostly transformed into the amorphous matrix, as shown in Fig. 5 [49]. Note that the volume fractions of the remaining nanocrystalline phases and the interdiffusion-induced amorphous matrix can be controlled by the applied ARB cycle, as depicted in Fig. 6 [51]. For example, if an alloy is designed to possess around 50% amorphous phase in Zr–Cu system, then about 80 ARB cycles are needed. At that time, the remaining nanocrystalline pure Zr or pure Cu phases are about 20 nm in size. The diffraction spots and rings in the TEM diffraction patterns of the ARB specimens are all originated from the pure elements, meaning that the nanocrystalline phases are those unmixed hard particles left from the previous severe
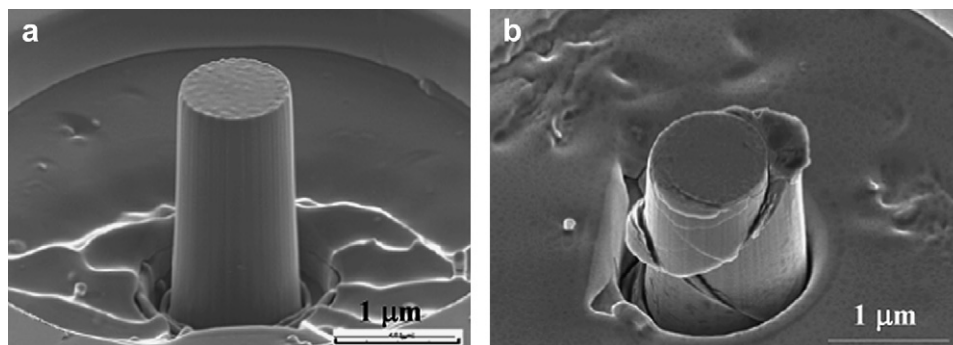
Fig. 8. Micro-pillars prepared by focus ion beam: (a) before micro-compression and (b) after micro-compression to about 30% strain [60].
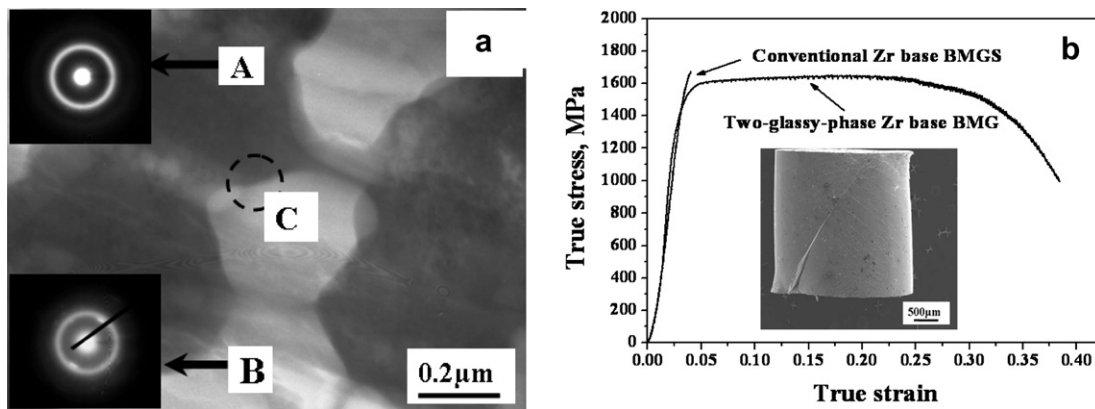
Fig. 9. (a) TEM bright-field image, with an inserted electron diffraction pattern, of the 2 mm Zr based BMG rod with micro-scaled phase separation, (b) room-temperature stress–strain curve for as-cast 2 mm diameter cylinders. The inset shows the deformed sample [21].

deformation and diffusion processes. A critical size of the nano-crystalline phases around 3 nm is consistently observed in all binary, ternary, and pentanary Zr–X based alloys, below the critical size a sudden transformation from the nanocrystalline to amorphous state would occur [50–54], as shown in Fig. 7 [50].

The friction stir process with effective liquid nitrogen cooling has also been adopted in preparing the MgAlZn intermetallic compound alloys, with nanocrystalline icosahedral particles plus a certain amount of amorphous phases [57,58].

4. Mechanical behavior

Extensive research has been devoted to the mechanical properties of BMGs, in an attempt to develop strong and tougher BMGs, as described below in Section 5. The effect of the compression specimen aspect ratio was examined in the Mg based BMGs [59]. Room-temperature compression tests are conducted on specimens with various height-to-diameter ratios (h/d) from 2:1, 1:1, 1:2, to 1:4. The failure strength, deformation strain, and the fracture surface morphologies are seen to vary systematically in accordance with the specimen h/d ratio. For specimens with h/d of 2:1 or 1:1, the compression response is similar to those in most reports. In contrast, for specimens with lower h/d ratios, especially at $h/d = 1:4$ (or 0.25), the shear band propagation appears to be constrained by the top and bottom platens, resulting in the enhanced ductility.

Micro-pillars with a diameter of 1 and 3.8 μm were fabricated from the Mg based metallic glasses using focus ion beam, and then tested in micro-compression at strain rates ranging from 6×10^{-5} to 6×10^{-1} s^{-1}, as shown in Fig. 8 [60]. The strength of the micro-pillars varies within 1342–1580 MPa, or 60–100% increment over that of the bulk specimens. This strength increase can be ratio-nalized using the Weibull statistics for brittle materials, and the Weibull modulus (m) of the Mg based metallic glasses is estimated to be about 35. The surface examination of the micro-pillar specimens indicates that the number of shear bands increase with the sample size and strain rates.

The specimen size dependence was also explored in the more ductile Zr based metallic glasses (with phase separation [21]), covering rod specimens with diameters of 2–4 mm down to micro-pillars with diameters of 0.7–4 μm [61]. The increment of strength is also analyzed in terms of the Weibull statistics. The extracted Weibull modulus is ~60 for this ductile phase-separated Zr BMGs [61], compared with the values ~35 and ~40 for the brittle Mg based BMGs [60] and $Au_{49}Ag_{5.5}Pd_{2.3}Cu_{26.9}Si_{16.3}$ BMG [62]. These results are consistent with other reported Weibull modulus values for the malleable $Zr_{48}Cu_{45}Al_7$ ($m = 73.4$) [63] and brittle $(Zr_{48}Cu_{45}Al_7)_{98}Y_2$ ($m = 25.5$) [63]. It seems that the size dependence is related to the ductility and cast defect of the amorphous alloys.

5. Toughening

The current critical issue for metallic glasses appears to be the toughening of their brittle nature. Based on previous efforts, the most promising approaches might be the enhancement of the
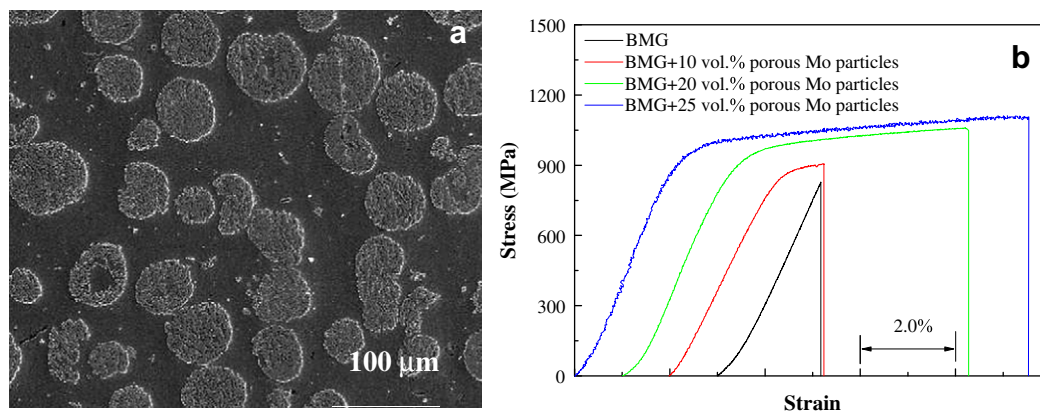
Fig. 10. (a) SEM micrograph of the homogeneous distribution of porous Mo particles in the Mg based bulk metallic glasses, with the inserted X-ray diffraction pattern, (b) representative room-temperature compressive engineering stress–strain curves for the as-cast 2 mm diameter compression specimens. The curves are shifted relative to each other for clarity [64].
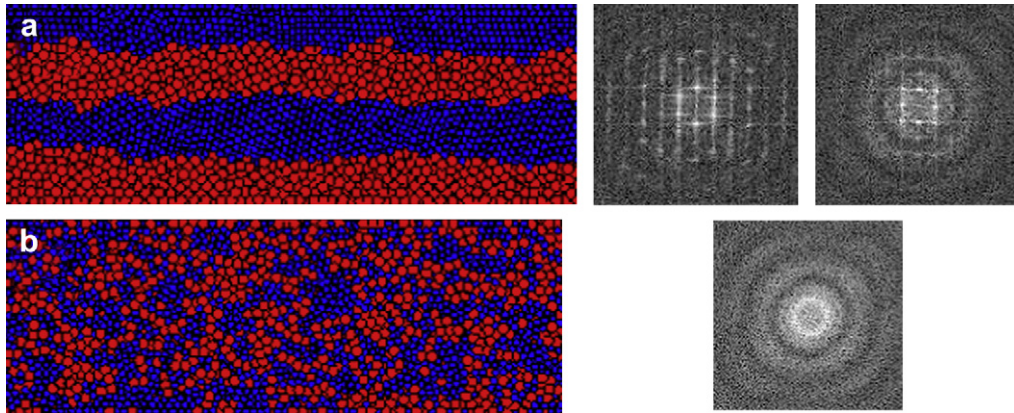
Fig. 11. The microstructural evolution and the associated two-dimensional Fourier transform of the bi-layered $Zr_{50}Ni_{50}$ model subjected to various ARB cycles: (a) initial state with the distinct Fourier transformed diffraction patterns for crystalline Zr and Ni, and (b) after 6 ARB cycles with the Fourier transformed diffraction patterns for an amorphous structure [54].

Poisson ratio by tailoring the compositions, the employment of in-situ phase separation to form an amorphous matrix mixed with a dendrite crystalline phase (forming a dendrite-reinforced amorphous composite) or a second glassy phase (forming a dual-phased glass) [21–23]. Tremendous efforts have been made in terms of the above approaches. One is to form liquid phase separation at high temperatures during induction melting, followed by rapid quenching to form the phase-separated glass. Successful results in Zr based glasses (e.g., $Zr_{63.8}Ni_{16.2}Cu_{15}Al_5$ or $Zr_{65.8}Ni_{15.8}Cu_{8.4}Al_{10}$) have achieved compressive ductility over 30%, as shown in Fig. 9 [21]. Another approach is to employ the porous particles into the amorphous matrix to form an amorphous matrix composite. Successful results in Mg based glasses added with 5–25 volume percent of porous Mo particles ($\sim$30–50 μm) have achieved compressive ductility over 10%, as shown in Fig. 10 [64]. Both these two approaches are designed with the concept in separating the homogeneous glassy matrix into numerous individual compartments with smooth but distinctive interfaces. The complicated interaction of propagating shear bands with these compartments and interfaces would promote multiple shear banding resulting in improved ductility.

The gain of high compressive strength and remarkable macroscopic plastic strain of 30% in the phase-separated $Zr_{63.8}Ni_{16.2}Cu_{15}Al_5$ or $Zr_{65.8}Ni_{15.8}Cu_{8.4}Al_{10}$ is attributed to the unique glassy structure correlated with the chemical inhomogeneity on the micron scale; the hard phases surrounded by the soft phases, leading to an inherent capability of extensive shear band formation, interactions, and multiplication [21–23]. The work shows that, by
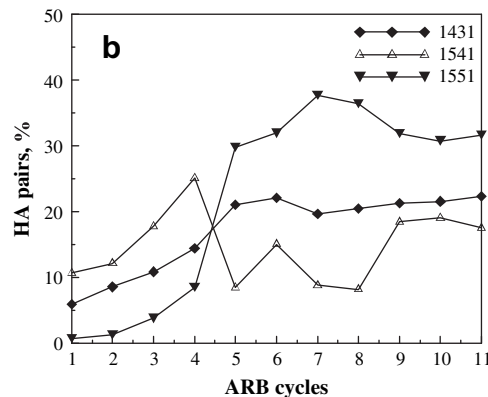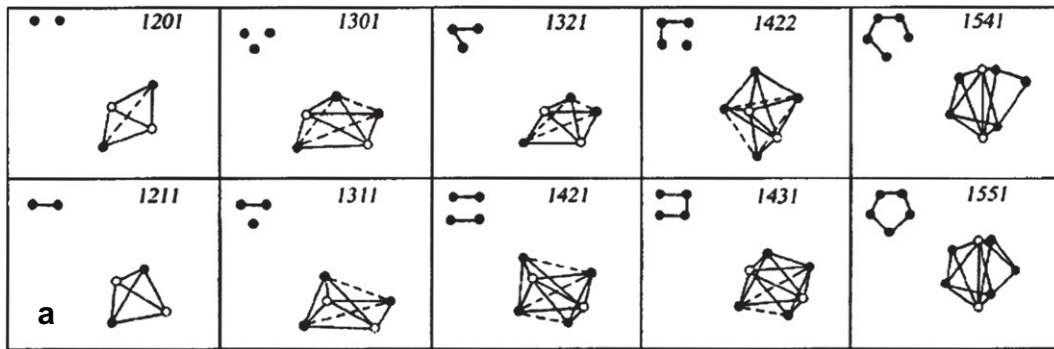
Fig. 12. (a) The schematic drawing of the related HA pairs [67]. (b) Variations of the HA indices of the Zr–Ni alloys during different ARB cycles: 1431, 1541, and 1551 [55].
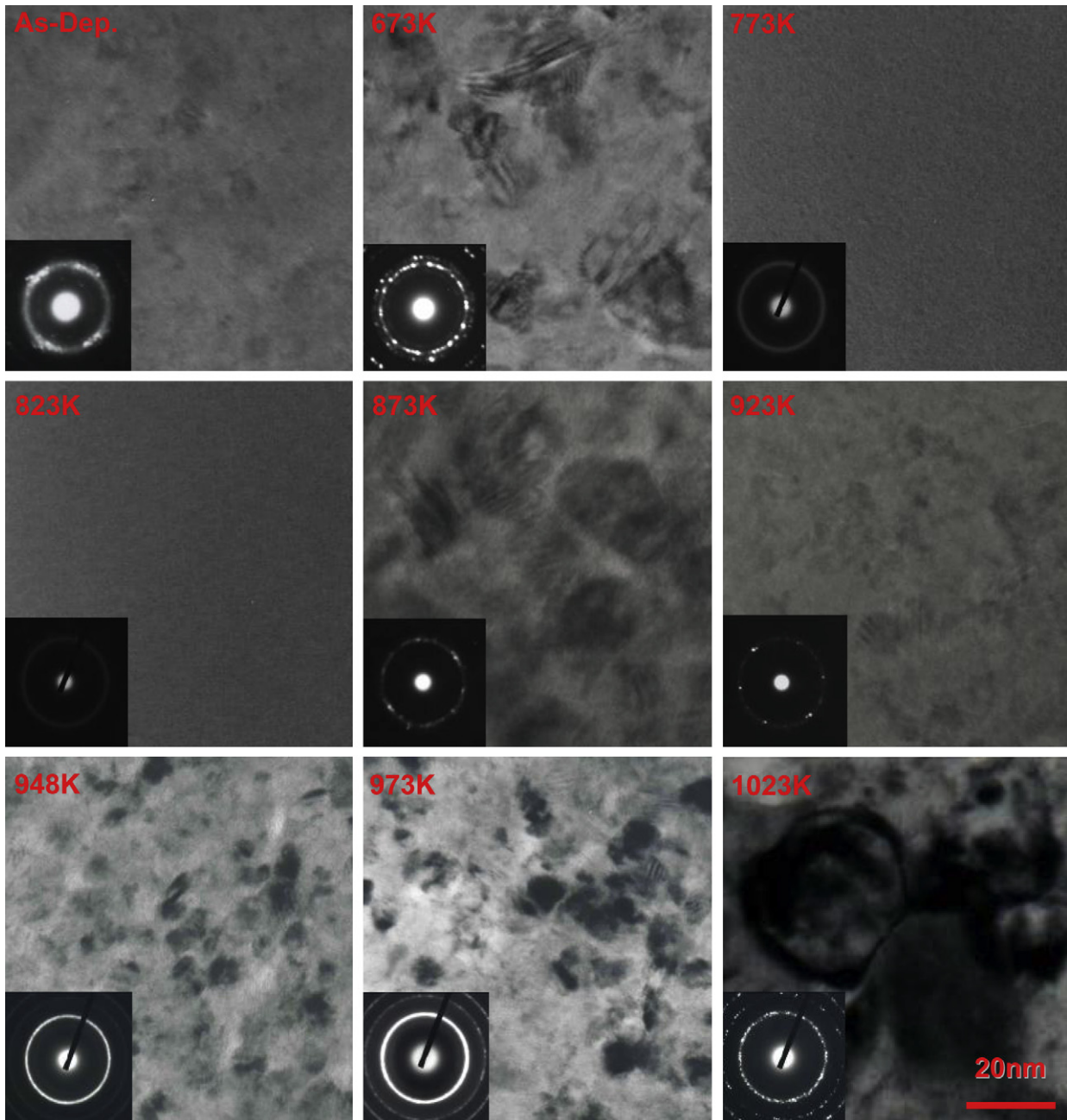
Fig. 13. Typical TEM bright-field images and diffraction patterns of the $Fe_{65}Ti_{13}Co_8Ni_7B_6Nb_1$ films in as-deposited and annealed conditions [69].

the two-liquid phase separation in accordance with the thermodynamic prediction, a good-GFA and ductile BMG can be achieved from the two-glassy phase microstructure.

Recent works on the Mg based BMGs added with micro-scaled Fe [65] or Ta [66] particles are under investigation. The BMGCs of these systems also show compression plasticity over 10%. The brittle nature of the Mg based BMGs can be sufficiently toughened by the Fe and Ta particles.

6. Modeling

Molecular dynamics (MD) simulation was applied for the structural evolution and mechanical response of the metallic glasses using the tight-binding potentials for the elements

[53–56]. For the simulation for the ARB solid-state vitrification process, the molecular dynamics simulation reveals that it needs only 6 cycles for a bi-layer structure, with 5 nm in each layer thickness, to fully transform into a completely amorphous state, as shown in Fig. 11 [54]. The potential energy between two distinct atoms increases during the transition between nano-crystalline and amorphous state due to the severe structure change. It increases the difficulty for atoms to maintain the crystalline structures. The values of the nearest neighboring distance extracted from the transmission electron microscopy (TEM) observation and the MD simulation are both smaller than the theoretically calculated value. A new tighter packing atomic structure in the $Zr_{50}Ni_{50}$ amorphous alloy is formed due to the large negative mixing enthalpy.
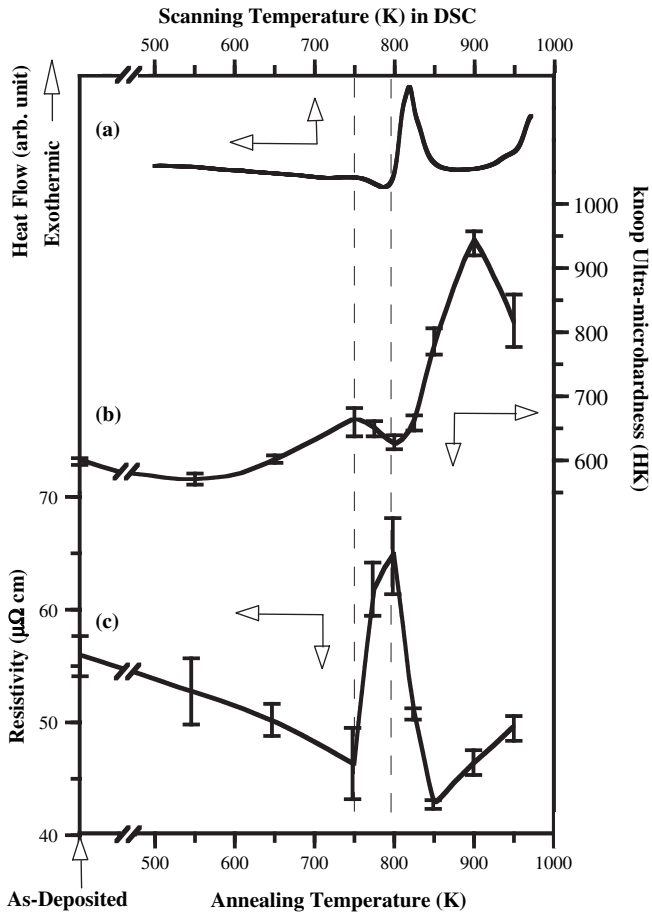
Fig. 14. (a) DSC thermogram of an as-deposited $Zr_{47}Cu_{31}Al_{13}Ni_9$ film; variations of (b) Knoop ultra-microhardness and (c) electrical resitivity with the annealing temperature. Approximate location of supercooled liquid region is marked by the dash lines to facilitate visual comparison [68].

The gradual vitrification evolution of atom mixing and local atomic pairing structure of the binary Zr–Ni alloy during severe deformation at room temperature is traced numerically by MD simulation in terms of the HA index (Fig. 12 [67,55]) developed by Honeycutt and Anderson [67]. It is found that the icosahedra clusters will gradually develop with increasing disorder environment of alloys. Other compound-like transition structures were also observed as transient in the Zr–Ni ARB couple during the solid-state amorphization process under severe plastic deformation. Since the time scale of the MD simulation is several orders of magnitude shorter than reality, the simulated atomic evolution can be viewed as that would occur at ultra-high strain rates. Simulation of the deformation behavior and shear band evolution during indentation, compression and fatigue loading is now undertaken.

7. Thin film metallic glasses

The vapor–solid quenching during sputtering enables the amorphous or nanocrystalline phases to form. The thin film amorphous alloys are generally called as the thin film metallic glasses (TFMGs), which can be prepared by many physical vapor deposition methods such as sputtering or evaporation. TFMGs might have tremendous application potentials in the areas of surface coating and MEMS [68,69]. Co-sputtering by two or three guns appears to be a promising process in studying the TFMGs with a wide variation of composition and microstructure.

It is also the first to report annealing-induced amorphization in glass-forming $Zr_{47}Cu_{31}Al_{13}Ni_9$ [68] and $Fe_{65}Ti_{13}Co_8Ni_7B_6Nb_1$ [69] films at a temperature within the supercooled liquid region (Fig. 13 [69]). The extensive amorphization is presumably attributed to sufficient thermal and interfacial energies between nanocrystallites and glassy matrix that are present in the as-deposited condition. The formation of comprehensive amorphous structure gives rise to notable alterations in the electrical, mechanical and magnetic properties of annealed films (Fig. 14 [68]). Important feature of these works is that a prominent strengthening effect is observed due to the amorphous matrix dispersed with nanocrystalline phases upon annealing. In addition, the glass-forming film coating is applied to improve the fatigue properties of material for the first time [70,71]. The excellent adherence and the smooth film surface have a noticeable influence on the fatigue life. With the deposition of the $Zr_{47}Cu_{31}Al_{13}Ni_9$ glass-forming film, the fatigue life of the 316L stainless steel could be increased by 30 times, and the fatigue limit could be elevated by 30%, depending on the maximum stress applied to the steel (Fig. 15 [70]). The high strength and the good bending ductility might be other important factors for the improvement.

In addition, the fully amorphous thin films can be easily prepared by co-sputtering of the Zr–Cu or Zr–Cu–Ti systems [72,73]. Partial amorphous thin films can be achieved by co-sputtering of Mg–Cu system [74], or multilayer sputtering plus post-annealing in the Zr–Cu system [72].

8. Oxidation and corrosion

The oxidation behaviors have been examined in the Fe, Ni, Zr and Mg based BMGs in Taiwan [75–82]. For the Fe based alloys, the $Fe_{72}B_{22}Y_6$ BMG and its crystalline counterpart were studied over the temperature range of 600–700 °C in dry air [75]. The results showed that the oxidation kinetics of both the glassy and crystalline alloys in general follow a parabolic rate law although a two-stage kinetics was noted at 700 °C for the glassy alloy. The oxidation rates of the two alloys increased with increasing temperature, and the parabolic rate constants of the glassy alloy are much lower than those of the crystalline counterpart. The scales formed on the glassy alloy consisted mainly of boron oxide (B_2O_3) and minor amounts of iron oxides (Fe_3O_4/FeO). Conversely, duplex scales formed on the crystalline counterpart were composed of an outer layer of Fe_2O_3 and an inner layer of Fe_3O_4–YBO_3 mixture. The formation of B_2O_3 is
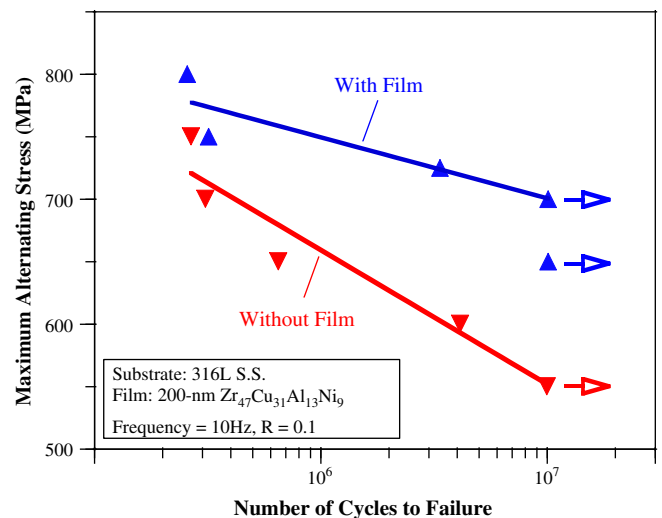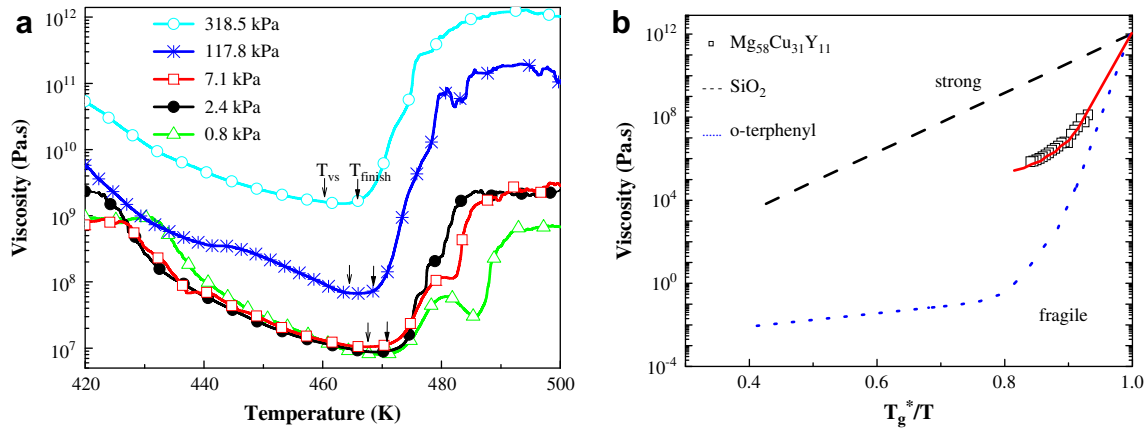

Fig. 15. Stress versus fatigue cycle for samples with and without the $Zr_{47}Cu_{31}Al_{13}Ni_9$ film. Arrows indicate the run-out data without the failure [70].

Fig. 16. (a) Temperature dependence of the effective viscosity for the indicated applied stress at a heating rate of 10 K/min. (b) The viscosity data on $Mg_{58}Cu_{31}Y_{11}$ (or the Angell plot). The data on the strong SiO_2 and fragile o-terphenyl glasses are compared with $Mg_{58}Cu_{31}Y_{11}$ [87].

responsible for the reduced oxidation rates of the glassy alloy as compared to those of crystalline counterpart.

The high-temperature oxidation behaviors of the Zr and Cu based BMGs in dry air or oxygen environment have been systematically examined by Kai and his group [76–82], including $Zr_{53}Ni_{23.5}Al_{23.5}$ at 400–600 °C [76], $Cu_{60}Hf_{25}Ti_{15}$ at 375–520 °C [77], $Cu_{60}Zr_{30}Ti_{10}$ and $Cu_{60}Zr_{20}Ti_{10}Hf_{10}$ at 350–500 °C [78], $(Cu_{78}Y_{22})_{98}Al_2$ amorphous composite at 400–600 °C [79] and other systems [80–82]. For the $Zr_{53}Ni_{23.5}Al_{23.5}$ system at 400–600 °C [76], the oxidation kinetics of the alloy follow the single- or two-stage parabolic rate law at $T \leq 500$ °C, but could be fitted by a three-stage parabolic law at 550–600 °C. They found the amounts of Al_2O_3 and monoclinic-ZrO_2 in the scales increase with the oxidation temperature. Based on the crystallographic and microstructural characterization results, they suggest more complicated oxidation kinetics at the temperature near T_g (such as 500 °C) and above; this might have resulted from the fact that crystallization of oxidation takes place simultaneously.

For the $Cu_{60}Hf_{25}Ti_{15}$ system at 375–520 °C [77], they found that the oxidation rates of the amorphous alloy are much higher than those of polycrystalline pure Cu, and suggested that the additions of Hf and Ti accelerate the oxidation reaction. To determine the oxidation mechanism of the alloy, marker studies performed at 425 °C for 72 h show that Pt markers were always located on the scale surface, indicating that the oxidation mechanism is involved mainly inward diffusion of oxygen. In addition, they detected $Cu_{51}Hf_{14}$ and Cu_3Ti_2 phases in X-ray diffraction (XRD) results, indicating the occurrence of phase transformation during the oxidation test. On comparing the $Cu_{60}Zr_{30}Ti_{10}$ and $Cu_{60}Zr_{20}Ti_{10}Hf_{10}$ systems at 350–500 °C [78], they found the addition of Hf slightly

reduces the oxidation rate of alloy at 350–400 °C while the reverse situation is observed at higher temperatures. The scales formed on both alloys were strongly composition dependent, consisting of mostly CuO/Cu_2O and minor cubic-ZrO_2 and $ZrTiO_4$ for the ternary BMG, and of CuO, cubic-ZrO_2, and $Zr_5Ti_7O_{24}$ for the quaternary BMG. They concluded that the formation of $ZrTiO_4$ and $Zr_5Ti_7O_{24}$ is responsible for the faster oxidation rates of these BMG alloys.

In addition, the oxidation of the $(Cu_{78}Y_{22})_{98}Al_2$ amorphous composite containing Cu_5Y at 400–600 °C was also examined [79]. It is found that the Cu_5Y-bearing composite has lower oxidation rates than those of the $(Cu_{78}Y_{22})_{98}Al_2$ amorphous and pure Cu. The XRD and scanning electron microscopy (SEM) characterizations on scales formed during oxidation reveal that the scales formed on the Cu_5Y-bearing composite consist of mainly hexagonal-Y_2O_3 and minor CuO. On the other hand, the scales on $(Cu_{78}Y_{22})_{98}Al_2$ amorphous alloy are largely Cu_2O and CuO with minor amounts of Y_2O_3. Accordingly, they concluded that the presence of Cu_2O is responsible for the poor oxidation properties of $(Cu_{78}Y_{22})_{98}Al_2$ amorphous alloy.

In addition to oxidation, the corrosion properties of the Pd, Fe and Cu based BMGs were also studied in Taiwan [83–86]. They evaluated the corrosion properties of these alloys in various aqueous solutions such as NaCl, HNO_3, H_2SO_4, and HCl. They found that the alloys in amorphous state normally have better corrosion properties than those of crystalline state. For example, after crystallization by vacuum annealing at 650 °C for 1 h, the corrosion resistance of the $F_{40}Ni_{38}B_{18}Mo_4$ alloy under its crystalline state becomes inferior to its amorphous state [83]. But for some other cases, they also reported that the corrosion resistance of amorphous alloy can be improved about two to three times by annealing.
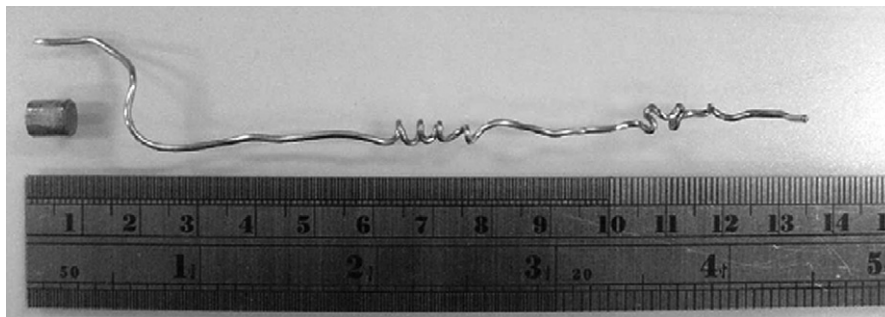
Fig. 17. A $Mg_{58}Cu_{31}Y_6Nd_5$ metallic glass wire with dimension of 1 mm in diameter and a length more than 160 mm fabricated by extruding the 6 mm diameter BMG rod at 458 K [90].

This is particularly found in the $Pd_{40}Ni_{40}P_{20}$ alloy [84]. Their XRD result of the annealed sample shows the presence of several phosphides and palladium which behave as inert phases mixed with noble metal to enhance corrosion resistance.

The corrosion behavior of the $Ni_{58}Ta_{36}Sn_6$ 1-mm BMG rods was measured in HCl aqueous solution, open to air at 25 °C. The polarization curve of pure tantalum is also displayed to contrast with the Ni–Ta–Sn BMG. In anodic region, the alloy spontaneously passivates. After a potential larger than 0.3 V, a passivation current density is noted as being slightly lower than that of pure tantalum. The open-circuit potential of the glassy alloy is about 0.13 V, being nobler than that of pure tantalum [75].

In addition, they studied hydrogen permeation of amorphous Fe based alloys, focusing on alloying element effects [85]. They pointed out that the apparent solubility of hydrogen in $Fe_{81}B_{13.5}Si_{3.5}C_2$ is higher than that in $Fe_{40}Ni_{38}B_{18}Mo_4$ because of the hydrogen-trapping effect of carbon and silicon atoms. They further reported that the presence of smaller atoms of carbon and silicon results in decreases in hydrogen permeation rate and effective diffusivity in the $Fe_{81}B_{13.5}Si_{3.5}C_2$ alloy. Moreover, they evaluated the corrosion behavior of mechanically alloyed $Cu_{60}Zr_{30}Ti_{10}$ BMG in different corrosive solutions using the potentiodynamic method [85]. The glassy alloy exhibits the most corrosion resistance in the

H_2SO_4 solution, while, in NaCl solution, there is the pit growth on the surface leading to breakdown of the passive film due to the galvanic corrosion mechanism [85].

9. Thermomechanical behavior

The viscous flow behavior of the $Mg_{58}Cu_{31}Y_{11}$ bulk amorphous rod in the supercooled viscous region is investigated using differential scanning calorimetry (DSC) and thermomechanical analyzer (TMA) [87]. Below the glass transition temperature, T_g, a linear thermal expansion coefficient of $3 \pm 1 \times 10^{-6}$ m/m K was obtained. In contrast, significant viscous deformation occurred as a result of a compressive load above T_g. The onset, semi-steady-state, and finish temperatures for viscous flow, determined by TMA, are slightly different from the glass transition and crystallization temperatures measured by DSC. All these characteristic temperatures decrease with increasing applied stress, suggesting accelerated crystallization in the present $Mg_{58}Cu_{31}Y_{11}$ under stress. The appropriate working temperature for micro-forming as determined by the semi-steady-state viscous flow temperature is about 460–474 K. The effective viscosity within this temperature range is estimated to be about 10^7–10^9 Pa s, and it increases with increasing applied stress, as demonstrated in Fig. 16(a) [87]. The viscosity behavior of the Mg based BMGs falls in-between
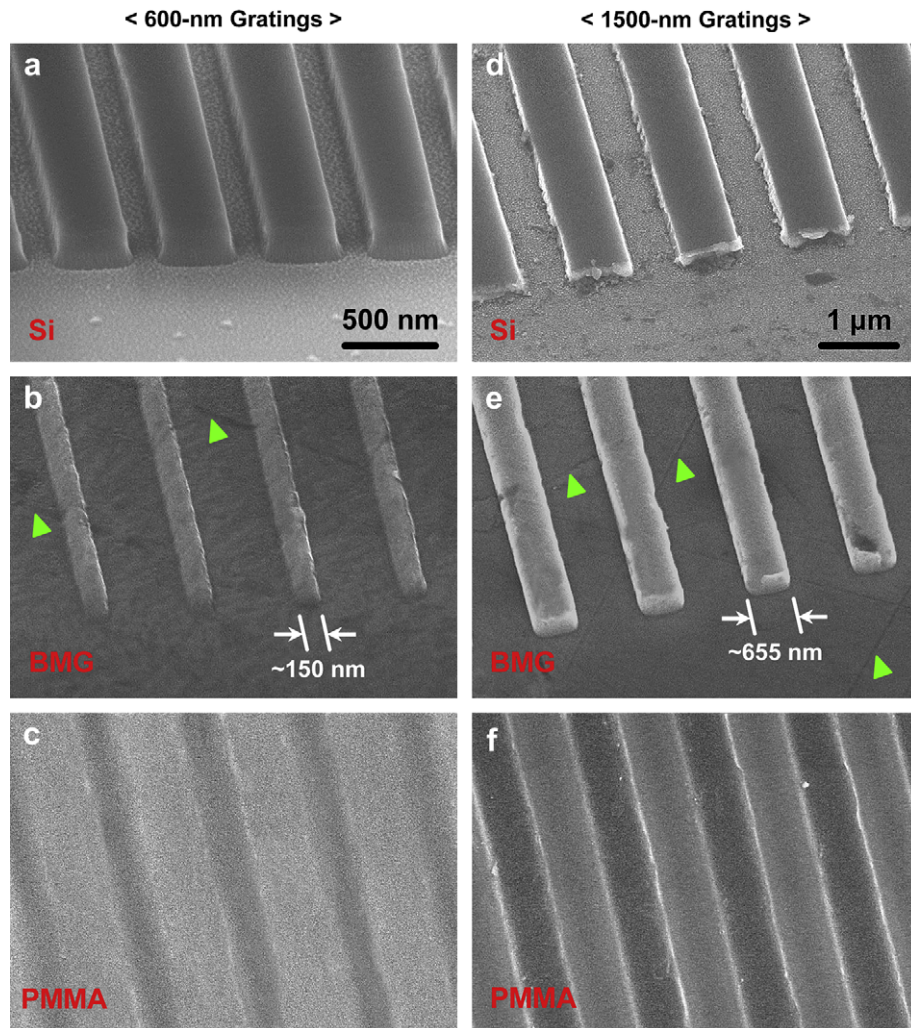
Fig. 18. SEM micrographs of the 600-nm (a,b,c) and 1500-nm (d,e,f) gratings in tilted view. The feature widths of 600-nm and 1500-nm $Pd_{40}Ni_{40}P_{20}$ BMG gratings are (b) ∼150 nm and (e) ∼655 nm, respectively. Green arrows indicate the polishing marks in BMG [95]. (For interpretation of the references to color in this figure legend, the reader is referred to the web version of this article.)
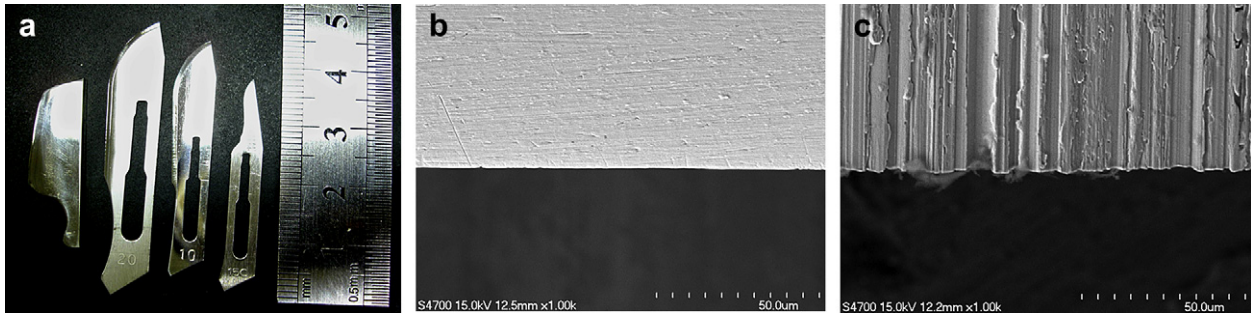
Fig. 19. (a) Appearance of Zr based BMG razor and commercial surgical razor. Enlarged knife edge of the blade: (b) Zr based BMG blade and (c) commercial S-15C blade [96].

the strong SiO_2 glass and the polymer o-terphenyl fragile glass, as shown in Fig. 16(b) [87].

The viscous flow behavior and thermomechanical properties of $Mg_{65}Cu_{25-x}B_xGd_{10}(x=0$ and 3 at%) [88] and $Mg_{65}Cu_{25-x}Ag_xGd_{10}$ $(x=0,3,10$ at%) [89] BMGs in the supercooled liquid region have also been investigated. It is found that the fragility of the supercooled liquid is reduced by the boron or silver addition, thus degrading the deformability. This conclusion is supported by the many other extracted parameters. The lowest viscosity was found in the base alloy, $Mg_{65}Cu_{25}Gd_{10}$, in the level of 10^6–10^7 Pa s. Thus, even with much higher hardness, the B- or Ag-additive Mg based BMG will be more difficult to be formed, which appears to be a negative factor in applying in the micro-forming or nano-imprinting industry.

With the relatively low viscosity between 10^6 and 10^7 Pa s within the supercooled temperature region of the $Mg_{58}Cu_{31}Y_6Nd_5$ BMG, a high plastic strain can be obtained easily by compression test within this temperature region. In addition, the XRD result shows that the $Mg_{58}Cu_{31}Y_6Nd_5$ BMG sample maintains its amorphous state after compression at 458 K and different strain rates. In parallel, a strain rate sensitivity exponent (m) close to 1.0 can be obtained for $Mg_{58}Cu_{31}Y_6Nd_5$ deformed at 448 K, 453 K and 458 K, suggesting an ideal Newtonian fluid superplasticity behavior. A 6 mm $Mg_{58}Cu_{31}Y_6Nd_5$ BMG rod was extruded at 458 K into a long wire for more than 160 mm in length, as depicted in Fig. 17 [90].

10. Forming and applications

Extensive plasticity (or superplasticity) of BMGs at temperatures within the supercooled liquid region has been studied extensively [91–94]. The alloys studied included the Pd, Zr, Cu, and Ce based BMGs. The superplastic-like behavior confirmed in the supercooled liquid region can be used to process imprints of nano- and micro-parts. A typical example is presented in Fig. 18 [95] for nano-grating using a Pd based BMG. It is demonstrated that nanostructured gratings with 600-nm and 1500-nm periods can be replicated with high fidelity on BMG in air using master Si dies. The grating features and diffraction properties of the first-generation BMG gratings are comparable to those of the original Si master dies, but the quality of replica depends on the feature size [95]. These replicated BMG gratings can be used as molding dies to further create the second-generation replicas on conventional polymethylmethacrylate (PMMA). This study shed lights on the possibility of nano-imprinting optical gratings on BMG in air and is a first step towards fabrication of integrated optical components such as diffractive optical nano-structured elements.

Potential application of the Zr based BMG can be extended to the medical tool such as the surgical razor or micro-surgery scissors. Because the razor made by the Zr BMG presents much smoother edge than the razor made by martensitic stainless steel. One example is shown in Fig. 19 [96].

Both the Zr based and Mg based BMGs present superior viscous flow behavior within their supercooled region. Therefore, these two BMGs can be applied to duplicate the hologram pattern via a micro-imprinting process. The replication of a hologram pattern with 100 nm depth was replicated by the $Mg_{58}Cu_{31}Y_6Nd_5$ BMG plate in the supercooled temperature region (Fig. 20) [90]. In addition, an imprinted hologram pattern with 0.6 μm depth also demonstrates extremely good micro-forming ability of the $(Zr_{53}Cu_{30}Ni_9Al_8)_{99.5}Si_{0.5}$ BMG, as shown in Fig. 21 [13].

The other attractive aspect in using BMGs for micro-forming is the relatively low forming temperature. The Mg [97–100] and Au based BMGs [100] have low glass transition temperatures in the
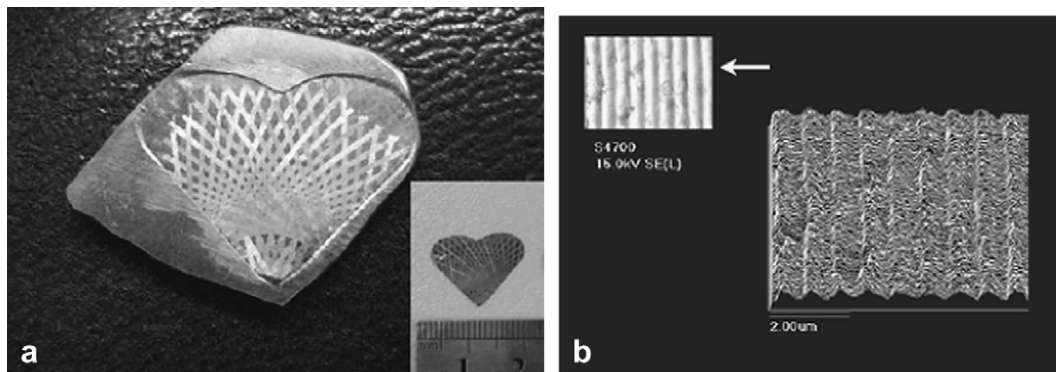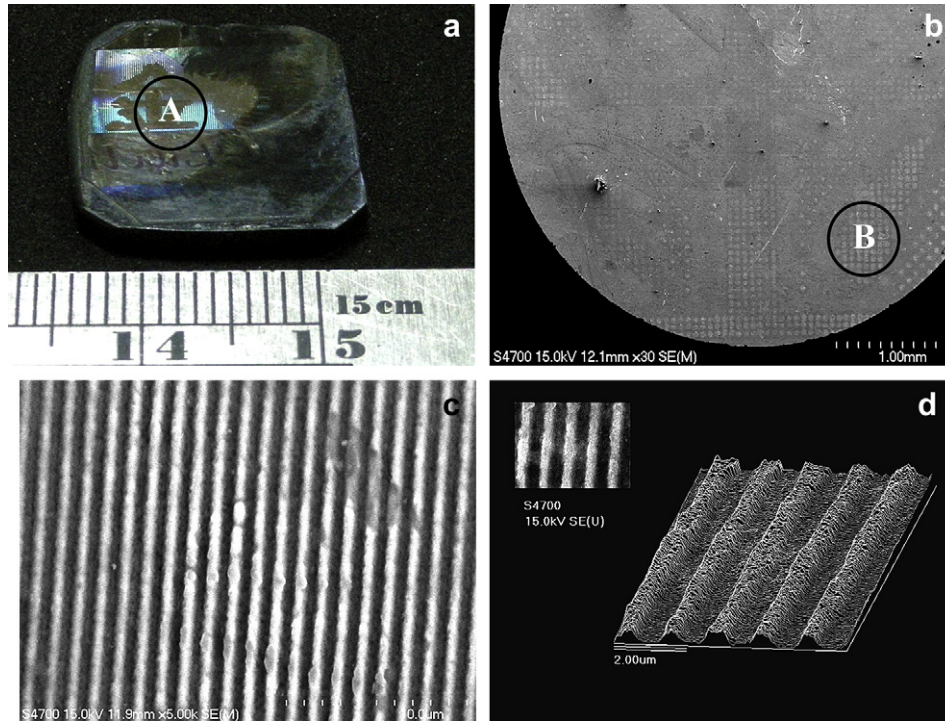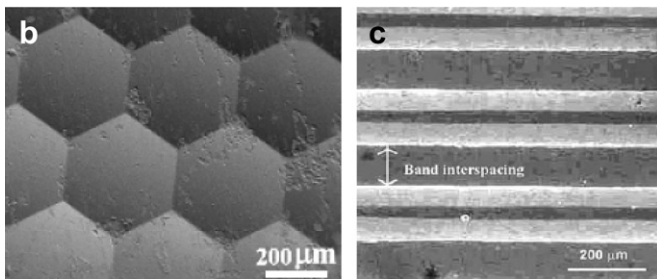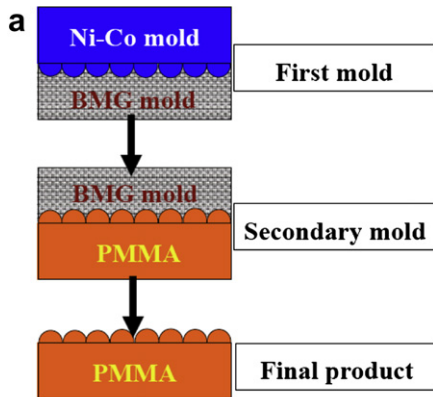

Fig. 20. The $Mg_{58}Cu_{31}Y_6Nd_5$ BMG photographs of (a) pre-engraved die and imprinted hologram pattern at 458 K, (b) secondary electron image of SEM and surface profile of the imprinted hologram pattern [90].

Fig. 21. (a) Photograph of imprinted hologram pattern of the $(Zr_{53}Cu_{30}Ni_9Al_8)_{99.5}Si_{0.5}$ BMG, (b) SEM images of circle A area in (a), (c) enlarged SEM image of circle B area in (b), and (d) surface profile of the imprinted hologram pattern [13].

range of 140–160 °C, making the viscous forming or imprinting easy to operate. The low forming temperature lies in the same temperature range for polymer materials such as PMMA, and the low forming temperature also prevent from the oxidation problem.

Fig. 22. (a) The schematic replication process first on BMG and then on the PMMA, (b) SEM micrograph showing the imprinted micro-lens, and (c) SEM micrograph showing the V-groove pattern [98].

The pressing can also be performed in air due to the low forming temperatures within 140–160 °C for the Mg and Au based BMGs. Successful micro-imprinting of the $Mg_{58}Cu_{31}Y_{11}$ BMGs have achieved for making hexagonal micro-lens arrays. The original convex Ni–Mo mold made by electro-plating is pressed onto the BMG at 140–160 °C for a few minutes at a low pressure in the range 0.1–1 MPa (Fig. 22(a) [98]) and the printed concave BMG mold is applied onto PMMA, forming a convex pattern. The results demonstrate that the imprinting is feasible and promising. The resulting hexagonal micro-lens arrays are shown in Fig. 22(b) [98]. Micro-scaled V-grove patterns (Fig. 22(c) [98]) can also be imprinted on the Mg [97–99] and Au based BMGs [100]. With the anti-oxidation, anti-corrosion, and good forming ability, the Au based BMG may be a material with high potential for micro-electromechanical systems (MEMS) applications.

Acknowledgment

References

[1] Inoue A. Stabilization of metallic supercooled liquid and bulk amorphous alloys. Acta Mater 2000;48:279.

[2] Wang WH, Dong C, Shek CH. Bulk metallic glasses. Mater Sci Eng R 2004;44:45.

[3] Schroers J, Pham Q, Desai A. Themoplastic forming of bulk metallic glass – a technology for MEMS and microstructure fabrication. J Microelectromech Syst 2007;16:240.

[4] Chen MW. Mechanical behavior of metallic glasses: microscopic understanding of strength and ductility. Annu Rev Mater Res 2008;38:14.1.

[5] Miller M, Liaw PK, editors. Bulk metallic glasses, an overview. NY: Springer; 2008.

[6] Jang JSC, Chen YW, Chang LJ, Cheng HZ, Huang JC, Tsau CY. Crystallization and fracture behavior of the $Zr_{65-x}Al_{7.5}Cu_{17.5}Ni_{10}Si_x$ bulk amorphous alloys. Mater Chem Phys 2005;89:122.

[7] Jang JSC, Chang LJ, Chen GJ, Huang JC. Crystallization behavior of the $Zr_{63}Al_{7.5}Cu_{17.5}Ni_{10}B_2$ amorphous alloy during isothermal annealing. Intermetallics 2005;13:907.

[8] Jang JSC, Lu SC, Chang LJ, Hung TH, Huang JC, Tsao CYA. Crystallization and thermal properties of Zr–Al–Cu–Ni based amorphous alloy added with boron and silicon. J Metastab Nanocryst Mater 2005;24–25:201.

[9] Jang JSC, Chen YW, Chang LJ, Cheng HZ, Huang JC, Tsao CYA. Crystallization kinetics of the $Zr_{61}Al_{7.5}Cu_{17.5}Ni_{10}Si_4$ alloy using isothermal DSC and TEM observation. J Non-crystal Solids 2006;352:71.

[10] Jang JSC, Lu SC, Chang LJ, Yang TH, Huang JC, Liu CT. Thermal stability and crystallization of Zr–Al–Cu–Ni based amorphous alloy added with boron and silicon. Intermetallics 2006;14:951.

[11] Hung TH, Huang JC, Jang JSC, Lu SC. Improved thermal stability of amorphous ZrAlCuNi alloys with Si and B. Mater Trans 2007;48:239.

[12] Chang LJ, Wang IH, Jang JSC, Chen GJ, Hung TH, Huang JC. Crystallization kinetics and thermal stability of the $Zr_{60}Al_{7.5}Cu_{17.5}Ni_{10}Si_4B_1$ alloy by isothermal DSC and TEM observation. Mater Sci Eng A 2007;449–451:511.

[13] Jang JSC, Chang CF, Huang YC, Huang JC, Chiang WJ, Liu CT. Viscous flow and microforming of a Zr-base bulk metallic glass. Intermetallics 2009;17:200.

[14] Lu ZP, Shen J, Xing DW, Sun JF, Liu CT. Appl Phys Lett 2006;89:071910.

[15] Chang LJ, Jang JSC, Yang BC, Huang JC. Crystallization and thermal stability of the amorphous $Mg_{65}Cu_{25-x}Gd_{10}Ag_x$ $(x = 0 \sim 10)$ alloys. J Alloys Compd 2007;434–435:221.

[16] Hung TH, Chang YC, Wang YN, Tang CW, Chen HM, Tsai YL, et al. Development of Mg based amorphous alloys with higher amounts of rare earth elements. Mater Trans 2007;48:1621.

[17] Jang JSC, Tseng CC, Chang LJ, Chang CF, Lee WJ, Huang JC, et al. Glass forming ability and thermal properties of the Mg based amorphous alloys with dual rare earth elements addition. Mater Trans 2007;48:1684.

[18] Chang LJ, Yang BC, Chiang PT, Jang JSC, Huang JC. Glass forming and thermal properties of the $Mg_{65}Cu_{25}Gd_{10-x}Nd_x$ $(x = 0 \sim 10)$ amorphous alloys. Mater Sci Forum 2007;539–543:2106.

[19] Cheng YT, Hung TH, Huang JC, Jang JSC, Tsao Chi CY, Lee PY. Effects of partial replacement of Cu and Y by boron in Mg–Cu–Y amorphous alloys. Intermetallics 2006;14:866.

[20] Cheng YT, Hung TH, Huang JC, Hsieh PJ, Jang JSC. The thermal stability and crystallization kinetics of Mg–Cu–Y–B alloys. Mater Sci Eng A 2007;449–451:501.

[21] Du XH, Huang JC, Hsieh KC, Jang JSC, Liaw PK, Lai YH, et al. Two-glassy-phase bulk metallic glass with remarkable plasticity. Appl Phys Lett 2007;91:131901.

[22] Du XH, Huang JC, Hsieh KC, Jang JSC, Liaw PK, Chen HM, et al. Mechanical properties of Zr-based two-glassy phase bulk metallic glass. Adv Eng Mater 2009. doi:10.1002/adem.200800370.

[23] Du XH, Huang JC, Chen HM, Chou HS, Lai YH, Hsieh KC, et al. Phase separated microstructure and shear banding behavior in a designed Zr based glass-forming alloy. Intermetallics 2009;17:607.

[24] Zhang T, Inoue A, Masumoto T. Mater Trans JIM 1991;32:1005.

[25] Du XH, Huang JC. A modified glass formation criterion for various glass forming liquids with higher reliability. Chin Phys Lett 2007;24:1335.

[26] Du XH, Huang JC, Liu CT, Lu ZP. New criterion of glass forming ability for bulk metallic glasses. J Appl Phys 2007;101:086108.

[27] Du XH, Huang JC. New criterion in predicting glass forming ability of various glass-forming systems. Chin Phys B 2008;17:249.

[28] Lin CY, Tien HY, Chin TS. Soft magnetic ternary iron-boron based bulk metallic glasses. Appl Phys Lett 2005;86:162501.

[29] Lee MC, Lin CY, Chin TS. High permeability mano-crystalline FeSiBTaAg ribbons obtained by direct casting. Intermetallics 2007;15:1564.

[30] Tien HY, Lin CY, Chin TS. New ternary Ni–Ta–Sn bulk metallic glasses. Intermetallics 2006;14:1075.

[31] Chang LR, Young JH, Jang JSC, Huang JC, Tsao Chi YA. Synthesis of the magnesium-based nano/amorphous-composite alloy powder by the combination method of melt-spinning and mechanical alloying. Key Eng Mater 2006;313:97.

[32] Jang JSC, Chang LJ, Young JH, Huang JC, Tsao Chi YA. Synthesis and characterization of the Mg-based amorphous/nano ZrO₂ composite alloy. Intermetallics 2006;14:945.

[33] Chang LJ, Young JH, Jang JSC, Huang JC, Tsao Chi YA. Mechanical properties of the Mg-based amorphous zincornia composite alloy. Mater Sci Forum 2007;539–543:925.

[34] Chang LJ, Fang GR, Jang JSC, Lee IS, Huang JC, Tsao Chi YA. Hot workability of the $Mg_{65}Cu_{20}Y_{10}Ag_5$ amorphous/nano ZrO_2 composite alloy within super-cooled temperature region. Key Eng Mater 2007;351:103.

[35] Chang LR, Fang GR, Lee LS, Jang JSC, Huang JC, Tsao Chi YA. Mechanical properties of the hot pressed $Mg_{65}Cu_{20}Y_{10}Ag_5$/nano-ZrO₂ based amorphous matrix composites. Mater Trans 2007;48:1797.

[36] Ted Guo ML, Tsao Chi YA, Jang JSC. Crystallization behavior of spray-formed and melt-spun $Al_{89}La_6Ni_5$ hybrid composites with amorphous and nanostructured phases. Mater Sci Eng A 2005;404:49.

[37] Ted Guo ML, Tsao Chi YA, Jang JSC, Huang JC. Microstructure evolution of spray-formed bulk hybrid composite and melt-spun ribbon hybrid composite consisting of amorphous and nanostructured phases of $Al_{89}Nd_4Ni_5Cu_2$. Intermetallics 2006;14:1069.

[38] Guo MLT, Tsao Chi YA, Huang JC, Jang JSC. Microstructure characteristics of spray-formed and melt-spun $Al_{85}Nd_5Ni_{10}$ and $Al_{89}La_6Ni_5$ bulk hybrid composites. Key Eng Mater 2007;351:1.

[39] Ted Guo ML, Tsao Chi YA, Huang JC, Jang JSC. Thermal stability and mechanical properties of spray-formed $Al_{89}La_6Ni_5$ bulk hybrid composites with amorphous matrix. Mater Trans 2007;48:1717.

[40] Chang KF, Guo MLT, Kong RH, Tsao Chi YA, Huang JC, Jang JSC. Mg–Cu–Gd layered composite plate synthesized via spray forming process. Mater Sci Eng A 2008;477:58.

[41] Lee PY, Lin CK, Jeng IK, Wang CC, Chen GS. Characterization of $Ni_{57}Zr_{20}Ti_{18}Al_5$ amorphous powder obtained by mechanical alloying. Mater Chem Phys 2004;84:358.

[42] Lee PY, Yao CJ, Chen JS, Wang LY, Jeng RR, Lin YL. Preparation and thermal stability of mechanically alloyed Cu–Zr–Ti–Y amorphous powders. Mater Sci Eng A 2004;375–377:834.

[43] Lin CK, Wang CC, Jeng RR, Lin YL, Yeh CH, Chu JP, et al. Preparation and thermal stability of mechanically alloyed Ni–Zr–Ti–Y amorphous powders. Intermetallics 2004;12:1011.

[44] Jeng IK, Lee PY. Synthesis of Ti-based bulk metallic glass composites containing WC particles. Mater Trans 2005;46:2963.

[45] Lee PY, Lo C, Jang JSC, Huang JC. Mg–Y–Cu bulk nanocrystalline matrix composites containing WC particles. Key Eng Mater 2006;313:25.

[46] Lee PY, Kao MC, Lin CK, Huang JC. Mg–Y–Cu bulk metallic glass prepared by mechanical alloying and vacuum hot-pressing. Intermetallics 2006;14:994.

[47] Lee PY, Liu WC, Lin CK, Huang JC. Fabrication of Mg–Y–Cu bulk metallic glass by mechanical alloying and hot consolidation. Mater Sci Eng A 2007;449–451:1095.

[48] Wu HM, Hung SS, Lee PY. Characterization of $Ni_{57}Zr_{20}Ti_{20}Sn_3$ amorphous powders obtained by mechanical alloying. J Alloys Compd 2007;434–435:386.

[49] Hsieh PJ, Hung YP, Huang JC. Transformation into nano-grained or amorphous state in Zr–X binary systems by accumulated roll bonding. Scr Mater 2003;49:173.

[50] Hsieh PJ, Hung YP, Chiu SY, Huang JC. Nanocrystallization and amorphization mechanisms in Zr–X alloys during accumulated roll bonding. Mater Trans (JIM) 2004;45:2686.

[51] Hsieh PJ, Huang JC, Hung YP, Chiu SY, Jang JSC. TEM characterization of nanocrystallization and amorphization evolution in Zr–X alloys during accumulated roll bonding. Mater Chem Phys 2004;88:364.

[52] Hsieh PJ, Huang JC, Jang JSC, Tsao CYA. Transformation between nano-crystallines and amorphous phases in Zr–X alloys during accumulative roll bonding. J Metastab Nanocryst Mater 2005;24–25:351.

[53] Hsieh PJ, Lo YC, Huang JC, Chu SP. On the latest stage of transformation from nanocrystalline to amorphous phases during ARB: simulation and experiment. Intermetallics 2006;14:924.

[54] Hsieh PJ, Lo YC, Wang CT, Huang JC, Chu SP. Cyclic transformation between nanocrystalline and amorphous phases in Zr based intermetallic alloys during ARB. Intermetallics 2007;15:644.

[55] Lo YC, Ju SP, Huang JC, Du XH. Atomic structural evolution of Zr–Ni during accumulative roll bonding using Honeycutt–Anderson (HA) pair analysis. Phys Rev B 2007;76:024103.

[56] Lo YC, Huang JC, Ju SP. Atomic structure evolution of Zr–Ti and pure Zr during accumulated roll bonding by HA pair analysis. Mater Chem Phys 2008;112:466.

[57] Chuang CH, Huang JC, Hsieh PJ. Using friction stir processing to fabricate MgAlZn intermetallic alloys. Scr Mater 2005;53:1455.

[58] Chang CI, Lee CJ, Chuang CH, Pei HR, Huang JC. On Mg–Al–Zn intermetallic alloys made by friction stir processing containing quasi-crystals and amorphous phases. Adv Mater Res 2007;15–17:387.

[59] Chen HM, Chang YC, Hung TH, Huang JC, Jang JSC, Liaw PK. Compression properties of Mg–Cu–Gd bulk metallic glasses with various specimen height to diameter ratios. Mater Trans 2007;48:1802.

[60] Lee CJ, Huang JC, Nieh TG. Sample size effect on the mechanical behavior of $Mg_{65}Cu_{25}Gd_{10}$ metallic glass. Appl Phys Lett 2007;91:161913.

[61] Lai YH, Lee CJ, Cheng YT, Chen HM, Chou HS, Du XH, et al. Bulk and microscale compressive properties of Zr-based metallic glass. Scr Mater 2008;58:890.

[62] Tang CW. MS Thesis, National Sun Yat-Sen University, Kaohsiung, Taiwan; 2008.

[63] Wu WF, Li Y, Schuh CA. Philos Mag 2008;88:71.

[64] Jang JSC, Ciou JY, Hung TH, Huang JC, Du XH. Enhanced mechanical performance of Mg based metallic glass with porous Mo particles. Appl Phys Lett 2008;92:011930.

[65] Jang JSC, Jian SR, Li TH, Huang JC, Tsao Chi YA, Liu CT. Structural and mechanical characterizations of ductile Fe particles reinforced Mg-based bulk metallic glass composites, J. Alloys Compd, submitted for publication.

[66] Jang JSC, Huang JC, Du XH. Plasticity enhancement of Mg-based bulk metallic glass with ductile Ta particles, unpublished research; 2008.

[67] Honeycutt JD, Andersen HC. J Phys Chem 1987;91:4950.

[68] Chu JP, Liu CT, Wang SF, Mahalingam T, O'Keefe MJ, Johnson B, et al. Annealing-induced full amorphization in a multicomponent metallic film. Phys Rev B 2004;69:113410.

[69] Chu JP, Lo CT, Fang YK, Han BS. On annealing-induced amorphization and anisotropy in a ferromagnetic Fe-based film: a magnetic and property study. Appl Phys Lett 2006;88:012510.

[70] Chiang CL, Chu JP, Liu FX, Liaw PK, Buchanan RA. A 200 nm thick glass-forming metallic film for fatigue-property enhancements. Appl Phys Lett 2006;88:131902.

[71] Liu FX, Liaw PK, Jiang WH, Chiang CL, Gao YF, Guan YF, et al. Fatigue-resistance enhancements by glass-forming metallic films. Mater Sci Eng A 2007;468–470:246.

[72] Chen CJ, Huang JC, Lai YH, Chou HS, Chang LW, Du XH, et al. On the amorphous and nanocrystalline Zr–Cu and Zr–Ti sputtered thin films. J Alloys Compd 2009. doi:10.1016/j.jallcom.2008.07.188.

[73] Chou HS, Huang JC, Chang LW, Nieh TG. Structural relaxation and nanoindentation response in Zr–Cu–Ti amorphous thin films. Appl Phys Lett 2008;93:191901.

[74] Chou HS, Huang JC, Lai YH, Chang LW, Du XH, Chu JP, et al. Amorphous and nanocrystalline sputtered Mg–Cu thin films. J Alloys Compd 2009. doi:10.1016/j.jallcom.2008.07.187.

[75] Hsieh HH, Kai W, Huang RT, Lin CY, Chin TS. Air oxidation of Fe$_{72}$B$_{22}$Y$_6$ bulk amorphous alloy at 600–700 °C. Intermetallics 2006;14:917.

[76] Kai W, Hsieh HH, Chen YR, Wang YF, Dong C. Oxidation behavior of an Zr$_{53}$Ni$_{23.5}$Al$_{23.5}$ bulk metallic glass at 400–600 °C. Intermetallics 2007;15:1459.

[77] Kai W, Hsieh HH, Ho TH, Huang RT, Lin YL. Air-oxidation behavior of a Cu$_{60}$Hf$_{25}$Ti$_{15}$ bulk metallic glass at 375–520 °C. Oxid Met 2007;68:177.

[78] Hsieh HH, Kai W, Jang WL, Huang RT, Lee PY, Wang WH. The oxidation behavior of Cu–Zr–Ti-base bulk metallic glasses in air at 350–500 °C. Oxid Met 2007;67:179.

[79] Kai W, Ho TH, Jen IF, Lee PY, Yang YM, Chin TS. Oxidation behavior of the (Cu$_{78}$Y$_{22}$)$_{98}$Al$_2$ bulk metallic glass containing Cu$_5$Y-particle composite at 400–600 °C. Intermetallics 2008;16:629.

[80] Kai W, Ho TH, Hsieh HH, Chen YR, Qiao DC, Jiang F, et al. Oxidation behavior of CuZr-based glassy alloys at 400–500 °C in dry air. Metall Mater Trans A 2008;39:1838.

[81] Hsieh HH, Kai W, Huang RT, Qiao DC, Liaw PK. Air oxidation of an Fe$_{48}$Cr$_{15}$C$_{15-}$Mo$_{14}$B$_6$Er$_2$ bulk metallic glass at 600–725 °C. Mater Trans 2007;48:1864.

[82] Hsieh HH, Kai W, Lin CY, Chin TS. Oxidation behavior of the Y$_{56}$Al$_{24}$Co$_{20}$ bulk amorphous alloy containing crystalline composites at 325–450 °C. Mater Sci Forum 2007;539–543:2117.

[83] Wu YF, Chiang WC, Wu JK. Effect of crystallization on corrosion behavior of F$_{40}$Ni$_{38}$B$_{18}$Mo$_4$ amorphous alloy in 3.5% NaCl solution. Mater Lett 2008;62:1554.

[84] Wu YF, Chiang WC, Chu JP, Nieh TG, Kawamura Y, Wu JK. Corrosion resistance of amorphous and crystalline Pd$_{40}$Ni$_{40}$P$_{20}$ alloys in aqueous solutions. Mater Lett 2006;60:2416.

[85] Chiang WC, Yeh WD, Wu JK. Hydrogen permeation in Fe$_{40}$Ni$_{38}$B$_{18}$Mo$_4$ and Fe$_{81}$B$_{13.5}$Si$_{3.5}$C$_2$ amorphous alloys. Mater Lett 2005;59:2542.

[86] Lin HM, Wu JK, Wang CC, Lee PY. The corrosion behavior of mechanically alloyed Cu–Zr–Ti bulk metallic glasses. Mater Lett 2008;62:2995.

[87] Chang YC, Hung TH, Chen HM, Huang JC, Nieh TG, Lee CJ. Viscous flow behavior and thermal properties of bulk amorphous Mg$_{58}$Cu$_{31}$Y$_{11}$ alloy. Intermetallics 2007;15:1303.

[88] Chang YC, Huang JC, Cheng YT, Lee CJ, Du XH, Nieh TG. Effect of silver or boron on viscosity and thermomechanical properties in Mg–Cu–Gd metallic glasses. J Appl Phys 2008;103:103521.

[89] Chang YC, Tang CW, Huang JC, Nieh TG. Viscous flow behavior and workability of Mg–Cu–(Ag)–Gd based bulk metallic glasses. Mater Trans 2008;49:2605.

[90] Jang JSC, Tseng CT, Chang LJ, Huang JC, Yeh YC, Jou JL. Thermoplastic forming properties and microreplication ability of a Mg-based bulk metallic glass. Adv Eng Mater 2008;10:1048.

[91] Chu JP, Chiang CL, Nieh TG, Kawamura Y. Superplasticity in a bulk amorphous Pd$_{40}$Ni$_{40}$P$_{20}$ Alloy: a compression study. Intermetallics 2002;10:1191.

[92] Chu JP, Chiang CL, Mahalingam T, Nieh TG. Plastic flow and tensile ductility of a bulk amorphous Zr$_{55}$Al$_{10}$Cu$_{30}$Ni$_5$ alloy at 700 K. Scr Mater 2003;49:435.

[93] Chiang CL, Chu JP, Lo CT, Nieh TG, Wang ZX, Wang WH. Homogeneous plastic deformation in a Cu-based bulk amorphous alloy. Intermetallics 2004;12:1057.

[94] Chu JP, Chiang CL, Wijaya H, Huang RT, Wu CW, Zhang B, et al. Compressive deformation of a bulk Ce-based metallic glass. Scr Mater 2006;55:227.

[95] Chu JP, Wijaya H, Wu CW, Tsai TR, Wei CS, Nieh TG, et al. Nanoimprint of gratings on a bulk metallic glass. Appl Phys Lett 2007;90:034101.

[96] Jang JSC, unpublished research work, I-Shou University, Kaohsiung, Taiwan; 2008.

[97] Pan CT, Wu TT, Chang YC, Huang JC. Experiment and simulation of hot embossing of a bulk metallic glass with low pressure and temperature. J Micromech Microeng 2008;18:025010.

[98] Pan CT, Wu TT, Chen MF, Hwang YM, Chang YC, Lee CJ, et al. Hot embossing of micro-lens array on bulk metallic glass. Sensors Actuators A Phys 2008;141:422.

[99] Chang YC, Wu TT, Chen MF, Lee CJ, Huang JC, Pan CT. Finite element simulation of micro-imprinting in Mg–Cu–Y amorphous alloy. Mater Sci Eng A 2008;499:153.

[100] Tang CW, Chang YC, Wu TT, Huang JC, Pan CT. Micro-forming of Au$_{49}$Ag$_{5.5}$Pd$_{2.3}$Cu$_{26.9}$Si$_{16.3}$ metallic glasses in supercooled region. Adv Mater Res 2008;47–50:266.